Nonlinear viscoelastic-plastic material modelling for the behaviour of ice in ice-structure interactions

Ying Xu [a,b], Zhiqiang Hu [c,*], Jonas Ringsberg [d], Gang Chen [a,e]

[a] State Key Laboratory of Ocean Engineering, Shanghai Jiao Tong University, Shanghai, China

[b] Collaborative Innovation Center for Advanced Ship and Deep-Sea Exploration, Shanghai Jiao Tong University, Shanghai, China

[c] School of Engineering, Newcastle University, Newcastle upon Tyne, NE1 7RU, UK

[d] Department of Mechanics and Maritime Sciences, Chalmers University of Technology, Gothenburg, Sweden

[e] Marine Design & Research Institute of China, Shanghai, China

Abstract

In this paper, a three-dimensional constitutive ice model with nonlinear viscoelastic and plastic components acting in series is proposed for the dynamic simulation of ice-structure interactions. The former component corresponds to a nonlinear Burgers model, in which the deviatoric behaviour is viscoelastic and the volumetric behaviour is elastic. The Burgers model is combined with the well accepted Glen's law and Ashby and Duval' law to describe the time-dependent behaviour and distribution in relaxation time. A hydrostatic pressure- and octahedral shear stress-dependent Tsai-Wu-type yield criterion is adopted to invoke the plastic state. The proposed ice model is assumed to be isotropic and is implemented in the commercial software LS-DYNA as a user-defined material. Verification of this model is implemented via simulations of creep and indentation experiments and via the simulation of a scenario of ice-rigid steel plate collision. The simulation of creep experiments shows that this material model can reflect the viscoelastic properties of ice quite well. The calculated contact force and pressure-area curves agree well with the results of indentation

Corresponding author.
E-mail address: zhiqiang.hu@ncl.ac.uk

experiments. And the ice-rigid steel plate collision example yields reasonable results, indicating that the proposed model has a good capacity for describing the brittle behaviour of ice. The numerical verification proves that the proposed ice material model has a wide range of potential applications.

Key words: ice-structure interaction; ice model; viscoelastic-plastic model; Burgers model; numerical simulation

1. Introduction

The exploration of Arctic sea routes and oil and gas resources has become a trend in recent years, driven by climate warming, technological development and economic benefits (Khon et al., 2010; Ostreng et al., 2013). These changes will make the activities of ships and marine structures more frequent in Arctic. However, ice-structure interactions may cause serious damage to marine structures and ships, even resulting in sinking in serious conditions such as collisions, as well as leakage of oil and natural gas (Hill, 2006). Numerical simulation is an important method to investigate ice-structure interactions, and one of the key difficulties is in establishing an accurate ice material constitutive model.

The mechanical characteristics of ice are complex, including elasticity, delayed elasticity, plasticity and brittleness. Ice shows different deformation characteristics under different conditions. The review of ice properties can be found in Barrette and Jordaan (2001) and Schulson and Duval (2009). The behaviour of ice is affected by many factors, such as temperature, loading rate, brine and porosity. For example, when temperature decreases or strain rate increases, the post-peak stress will decrease quickly with strain and the ice deformation will transit from ductile region to brittle region as shown in Fig. 1. Therefore, establishing a relatively complete constitutive model has always been a challenging task. Most models contain only parts of the ice characteristics, and only a small portion of the models have been used in Finite Element tools to simulate ice-structure interaction.

For the spatial scale, ice-structure interaction is concerned with global ice loads and local ice loads. The former represents the resultant force on the structure and is related to the design of overall structure (Timco and Sudom, 2013). While the local ice loads are applied on a small and defined portion of a large area, and is related to the local structure to be designed. The process simulated in this paper is this kind of local ice-structure interaction, with ice load acting on a panel or plating between frames (Jordaan et al., 2005). The contact area is smaller than $3m^2$ in the simulation part of this paper. Masterson et al. (2007) proposed a local pressure-area curve applying to contact area less than $10m^2$, obtained from field measurement, small and medium scale indentation experiments. ISO Standard (2010) adopted this relation and it is used for comparison in Section 4.2 and Section 4.3. For the ice behavior and failure process in the local ice-structure interaction, Jordaan (2001) proposed a systematical elaboration to describe it. Ice loads are mainly transmitted to the structure through high-pressure zones (90% according to Johnston et al. (1998)). Ice of high-pressure zones is under high confinement due to the surrounding ice and structure and cracks are suppressed, so the ice there is highly damaged with recrystallization and will be crushed and extruded. While the ice around high-pressure zones fails in a brittle manner. Ice is at a relatively high strain rate in common ice-structure interactions, such as collision scenarios where ice strain rate is higher than 10^{-3}/s according to Liu et al. (2011), except for structures subjected to creep of level ice, especially when the temperature rises, where the ice strain rate is relatively low (lower than 10^{-5}) and ductile deformation dominates. In addition, confinement also influences the ice behavior. Even for ice-structure interaction in high rates, the ice of high-pressure zones deforms in a ductile manner with damage.

One type of the existing ice material models is the ones with physical basis. These models emphasize the description of internal microscopic changes of ice, such as crystal dislocations, grain boundary sliding, micro-cracks, cracks propagation and interaction, which need further experimental research of the

66 micromechanics and is still in the initial stages. Some physical based material models can be referred to Cole
67 (1995), Cole (1998), Kolari (2013) and Kolari (2017). Another main type is the phenomenological models
68 based on the theory of viscoelasticity/plasticity (Leclair et al. 1999) to describe the macroscopic phenomenon
69 (relation between stress, strain, time, etc.) other than the microscopic mechanism inside ice. A model
70 represented by rheological elements including springs and dashpots is an effective method and is also the
71 way to establish the material model in this paper.
72

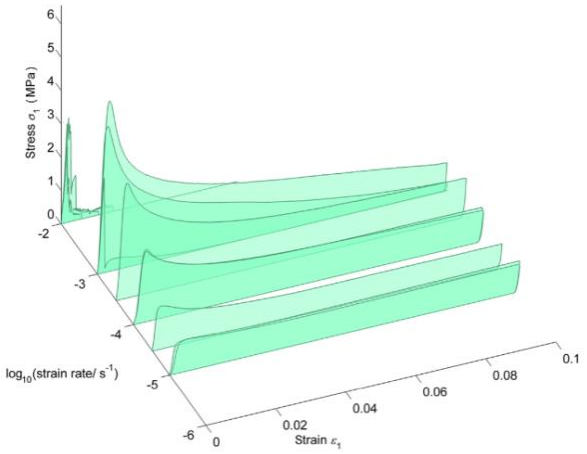

73

74 Fig. 1. Stress-strain curves at different strain rates from ductile to brittle zones (Snyder et al. 2016).

75 There have been many researches about the viscoelasticity/viscoplasticity of ice. Experimental studies
76 have shown that the ice continuum deformation is composite. According to the features (whether
77 time-dependent, recoverable), the ice deformation can be decomposed into instant elastic, delayed elastic
78 (growing with time at constant stress and recoverable) and viscous or plastic deformation (irrecoverable).
79 Glen (1955) proposed an equation related with temperature to describe the relation between viscous strain
80 rate and stress and is well accepted. Many laboratory experiments have been conducted since 1970s to
81 investigate the ice continuum deformation and used Glen' law to describe the viscous behaviour, and relevant
82 mechanical parameters were obtained, see, e.g., Barnes (1971), Jones, (1982), Mellor and Cole (1982), Sinha

(1982), Jones and Chew (1983), Durham et al. (1983), Rist and Murrell (1994), Gagnon and Gammon (1995), Schulson and Nickolayev (1995), Jones et al. (2003). Jellinek and Brill (1956) adopted a one dimensional Maxwell-Voigt model to describe the viscoelastic deformation of ice. Because the delayed elastic strain of ice display a distribution of retardation times, a large number of Kelvin units acting in series can capture this behavior. Xiao (1997) used one Maxwell unit and three Kelvin units to simulate the viscoelastic deformation and applied the model to Finite Element Analysis to take numerical simulations and compared the results with creep experiments. The results corresponded with the tested curves and the distribution of recovering strain in unloading phase was also simulated successfully. However, more rheological units bring more mechanical parameters need to be determined through experiments, and this makes the application of this type of model difficult. Leclair et al. (1999) applied an equation originally used for creep of polymeric material to simulate the viscoelastic deformation of ice, and obtained the parameters through cycle loading experiments. Ji et al. (2005) and Gang et al. (2006) established two viscoelastic-plastic models with Mohr-Coulomb yielding criterion and Drucker-Prager yield criterion respectively, the delayed elastic deformation was represented by Kelvin unit. The models were applied to simulate ice dynamics using smoothed particle hydrodynamics (SPH). It was found the singular problem in the Mohr–Coulomb yield criterion was overcame by the Drucker-Prager criterion. Some studies suggest that the Tsai-Wu type of yield criterion is more suitable for describing the behavior of ice, e.g., Riaka and Frederking (1987), Varsta (1983). Derradji-Aouat (2003) summarized and analyzed ice strength data of the previous experiments and used multiple elliptical surfaces to describe the failure of ice. Zhou et al. (2016) conducted experiments on columnar ice and adopted initial yield、hardening and subsequent yield to describe the ice behavior. It was found that the initial and subsequent yield surfaces maintained elliptical shape in the plane of effective stress versus hydrostatic stress.

105 Some models were combined with continuum damage theory representing micro-cracks to simulate the
106 quasi-brittle behavior of ice. Ortiz et al. (2015) adopted the elastic Mazars damage model to describe the
107 fragile response of ice, and the compressive failure of ice cylinders under high speed loading was simulated.
108 Taylor and Jordaan (2014) used Schapery's damage theory and element erosion techniques in Finite Element
109 Method to simulate the brittle process of ice and obtained the contact pressure-time curve. Saksala et al.
110 (2015) combined continuum damage and embedded discontinuity to describe the strain-stress relation of ice.
111 Two dimensional simulations were conducted and the strain softening behaviour can be simulated. However,
112 damage based models need a robust material model without damage to completely describe ice behaviors
113 (Leclair et al., 1999), and these brittle models usually ignored the capacity of simulating viscoelasticity,
114 especially the delayed elastic behaviour. In fact, all these characteristics are included in ice material, one or
115 more features will be evoked in a given scenario and there is no definite boundary between these
116 characteristics. And the lack of ability to describe viscoelastic behavior limits the scope of application of the
117 model. Conditions with higher temperature, slow interaction, high confinement (such as high-pressure zones)
118 cannot be simulated. Therefore, it is meaningful to establish a comprehensive model that can be applied to a
119 wider range of scenarios.

120 The main objective of this study is to establish a comprehensive three-dimensional ice constitutive
121 model that can be used in Finite Element Method based on viscoelastic-plastic theory to simulate the
122 ice-structure interaction. The viscoelastic behaviour is described with an improved Burgers model (one
123 Maxwell and one Kelvin units acting in series), which is based on the laws summarised from experimental
124 results and takes the influence of temperature and confining pressure into account, thus can reflect the
125 viscoelastic behaviour of ice more accurately. The viscous relation is based on Glen's law (1955), and the
126 delayed elastic relation is based on Ashby and Duval' law (1985). The deviatoric and volumetric parts are

127 constructed separately. A Tsai-Wu type criterion is adopted to evoke the plastic deformation, and an empirical
128 failure criterion based on the effective plastic strain and hydrostatic pressure is adopted to determine the
129 failure of ice elements. In general, plastic theory is used to describe the ductile behaviour of ice. For the
130 numerical simulation of ice-structure interaction, the plastic theory can be applied to brittle region for
131 predicting the ice load in a proper way. Liu (2011) proposed an elastic-plastic model with the combination of
132 element erosion to simulate ice-ship collision scenario and the ice load was well predicted. In addition, plastic
133 theory based ice model has a potential for further development. It can be developed to model the post-peak
134 softening behaviour and the ductile-brittle transition of ice. Therefore, the model proposed in this paper can
135 reflect the viscoelasticity of ice and also can simulate the ice load of collision where ice fails mainly in brittle
136 region.

137 This model can be used for the simulation of isotropic freshwater ice and iceberg ice with low brine
138 content. Two typical experiments conducted on ice including a creep experiment and a medium-scale
139 indentation experiment, and a collision scheme between ice and a rigid plate were simulated to verify the
140 performance of this model. It is shown that the proposed ice model can simulate the comprehensive
141 characteristics during the ice-structure interaction scenario. The proposed ice model can be applied in FEM
142 simulations to give structural safety assessments for Arctic ships during their design phases or provide
143 evaluations for other ice-structure interaction-related engineering practices.

144 **2. Description of the constitutive viscoelastic-plastic ice material model**

145 The ice model proposed in this paper is an incremental viscoelastic-plastic model. The viscoelastic
146 constitutive law corresponds to a nonlinear Burgers model. The yield criterion marking the beginning of the
147 plastic phase corresponds to the Tsai-Wu yield surface, and the associated flow rule is adopted. The
148 numerical implementation is based on a differential method and return mapping algorithm.

2.1 Viscoelastic-plastic constitutive law for ice material

The deformation of ice are composed of several components: instantaneous elastic, delayed elastic, viscous, and plastic components. Fig. 2 illustrates the typical one dimensional ice creep behaviour, including the characteristics of the generation and recovery of the first three deformation components under a constant external force. The instantaneous elastic strain (ε^e) often makes up a small portion of the total strain of ice and it's reversible and time independent. It is followed by a period of transient creep which is composed of delayed elastic strain (ε^d) and viscous strain (ε^v), and then a steady-strain rate stage where the viscous strain dominates. The delayed elastic strain manifests as a gradually increasing strain for which the increase slows with time and the strain can also fully recover. And after the external load is removed, the deformation will relax with a distribution of relaxation times rather than a single relaxation time, manifesting as the fully recovery of this deformation will take a much longer time than it's generation (Leclair et al. 1999). The viscous strain is very small initially but becomes greater over time. For the creep deformation of granular polycrystalline ice, dislocation glide is usually the main mechanism, and dislocation climb is considered as a complementary mode (Schulson and Duval, 2009; Barnes, et al. 1971). The dislocation relaxation mechanism dominates the delayed elastic deformation of ice (Cole, 1995).

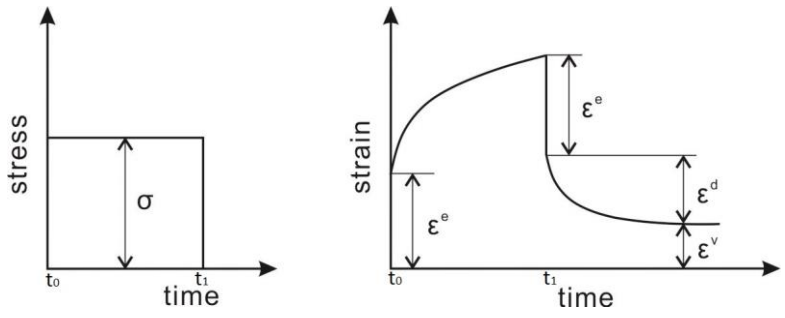

Fig. 2. Constant stress-time curve (left). Creep strain-time curve under the constant stress (right). Creep strain is composed of elastic strain, delayed elastic strain and viscous strain, and after the external force is removed after t_1, the elastic strain recovers immediately and the delayed elastic strain recovers with a distribution of

relaxation times.

Plastic strain and viscous strain are both permanent but behave in different ways in this study. Viscous strain is attributed to the time effect, and even with a small external force, it will occur. The plastic strain will only be produced on the condition that the ice exceeds its elastic limit or yield limit. That being the case, the yield criterion and flow rule are important for the plastic strain, and this will be discussed in the next section.

For the ice behaviour in a tri-axial stress state, the deformation mechanism of ice can be divided into two components: volume change and shape change of the ice crystal lattice. The volumetric deformation of ice is caused by the variation of the intermolecular distance under hydrostatic pressure, but the shape of the ice crystal remains the same. The deviatoric strain is attribute to the shape distortion of ice crystals, corresponding to the effect of deviatoric stress (Barrette and Jordaan, 2001). To facilitate the establishment of a constitutive model in a tri-axial stress state, the ice behaviour can be decomposed into these two parts to process separately.

According to the above phenomena, the material model proposed in this paper will be based on the following hypotheses：

- The material model is isotropic.
- The total deviatoric strain is assumed to be represented as the sum of instantaneous elastic strain, viscous strain, delayed elastic strain and plastic strain.
- The volumetric behaviour is represented by elastic and plastic strain.
- The viscous elastic and delayed elastic deformation will be affected by temperature.

Therefore, the total stress and strain tensors of ice can be decomposed into deviatoric part and volumetric part,

$$\varepsilon_{ij} = e_{ij} + \delta_{ij}\varepsilon_{vol} \tag{1}$$

$$\sigma_{ij} = s_{ij} + \delta_{ij} p \tag{2}$$

$$\delta_{ij} = \begin{cases} 1, & i = j \\ 0, & i \neq j \end{cases} \tag{3}$$

where ε_{ij} and σ_{ij} are the strain and stress components, e_{ij} and s_{ij} are the deviatoric strain and stress components, $\varepsilon_{vol} = \varepsilon_{ii} / 3$ and $p = \sigma_{ii} / 3$ are the volumetric strain and stress, and the Einstein summation convention (Lai et al. 2009) applies.

The total deviatoric strain rate $\dot{e}_{ij}$ and volumetric strain rate $\dot{\varepsilon}_{vol}$ can be expressed as,

$$\dot{e}_{ij} = \dot{e}_{ij}^{e} + \dot{e}_{ij}^{v} + \dot{e}_{ij}^{d} + \dot{e}_{ij}^{p} \tag{4}$$

$$\dot{\varepsilon}_{vol} = \dot{\varepsilon}_{vol}^{e} + \dot{\varepsilon}_{vol}^{p} \tag{5}$$

where $\dot{e}_{ij}^{e}$, $\dot{e}_{ij}^{v}$, $\dot{e}_{ij}^{d}$ and $\dot{e}_{ij}^{p}$ are the deviatoric elastic, viscous, delayed elastic and plastic strain rates, respectively, and $\dot{\varepsilon}_{vol}^{e}$ and $\dot{\varepsilon}_{vol}^{p}$ are the volumetric elastic and plastic strain rates, respectively. For the deviatoric viscoelastic behaviour including the first three parts, a Burgers model consisting of a Maxwell unit and a Kelvin unit arranged in series is used here. Fig. 3 shows the Burgers model. Elastic strain ε^{e} and viscous strain ε^{v} are represented by the spring and dashpot in Maxwell model, respectively. Delayed elastic strain ε^{d} is represented by the combination of spring and dashpot arranged in parallel in the Kelvin unit.

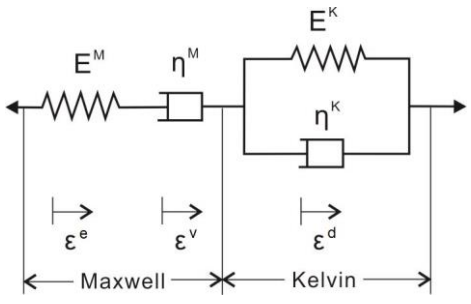

Fig. 3. One-dimensional Burgers model consisting of a Maxwell model and a Kelvin model arranged in series. Spring in the Maxwell model represents for the elastic strain, dashpot in the Maxwell model represents for the viscous strain, Kelvin model represents for the delayed elastic strain.

208 2.1.1 Elastic strain

209 The elastic volumetric strain has a linear relation to the volumetric stress, as does the deviatoric

210 instantaneous elastic strain with the stress components. The elastic part can be described by the generalized

211 Hooke's law,

212 $$\varepsilon_{vol}^{e} = \frac{p}{3K} \tag{6}$$

213 $$e_{ij}^{e} = \frac{s_{ij}}{2G^{M}} \tag{7}$$

214 where K is the bulk modulus and G^{M} is the shear modulus of the Maxwell unit.

215 2.1.2 Viscous strain

216 Basic viscous relation can be described as a linear relation between stress and strain rate according to

217 Newton's law ($\sigma = \mu\dot{\varepsilon}$), which also can be represented by the dashpot in original Maxwell unit. However,

218 many experiments have observed that the viscous strain rate is nonlinear with stress. Such as in constant

219 stress loading experiments, the viscous strain under different stress levels is in nonlinear relationship with

220 stress at the same loading time. Glen's law (1955) is a well-accepted equation to describe this relation. In this

221 paper, the formula proposed by Jones and Chew (1983) which was based on Glen's law and took confining

222 pressure into account is adopted to improve the Burgers model,

223 $$\dot{\varepsilon}_{v} = A\exp[-(Q+pV)/RT](\sigma_1-\sigma_3)^{n} \tag{8}$$

224 where $(\sigma_1-\sigma_3)$ is uniaxial stress, A and n are material constants，Q is activation energy, R = 8.314J/(mol·K)

225 is molar gas constant，T is absolute temperature, p is the hydrostatic pressure and V is the activation

226 volume. In order to extend this relation to three-dimension, the differential stress $(\sigma_1-\sigma_3)$ can be replaced

227 by effective stress according to the isotropic assumption, and the axial viscous strain rate can be written in the

228 deviatoric form.

229 $$\dot{e}_{ij}^{v} = \frac{s^{n-1}}{2\eta^{M}} s_{ij} \tag{9}$$

$$2\eta^{M} = A^{-1}\exp\left[\frac{Q+PV}{RT}\right] \quad (10)$$

where s_{ij} is deviatoric stress; $s=\sqrt{\frac{3s_{ij}s_{ij}}{2}}$ is the effective stress and the Einstein summation convention (Lai et al. 2009) applies. According to Jones and Chew (1983), V equals 32cm^3/mol here. The above stress unit is MPa.

In this equation, the influence of temperature is included. It is reflected in two parameters: temperature (T) and activation energy (Q). At the same stress level, the viscous strain rate improves and ice becomes softer as temperature increases. A lot of tri-axial experiments were conducted in the past decades, and many of the experimental data were analysed using Glen's law (1955), e.g., Durham et al. (1983), Barnes et al. (1971), Jones (1982), Rist and Murrell (1994). The values of the parameters were obtained and this provides a good reference for the determination of the parameters in the application of this model. It was found that n is around 3 under lower stress level, and could be 4 under higher stress level, which is probably associated with the occurrence of micro-cracking and non-basal gliding (Rist and Murrell, 1994). Q has different values in different temperature intervals, and some of the experimental suggestions are listed in Table 1.

Table 1. Values of Q from different experimental studies.

	Barnes et al. (1971)	**Barnes et al. (1971)**	**Sinha (1978)**	**Rist and Murrell (1994)**	**Budd and Jacka (1989)**
T (ºC)	< -8	-8 ~ -2	-5 ~ -45	-20 ~ -45	-10
Q (kJ/mol)	76.8	120	67	69	77

The creep tests simulated subsequently in this paper was conducted under -11°C and the effective stress was under 10MPa, thus 3 is an ideal value for n. And Q = 78.6kJ/mol and A = 6.5E8 s^{-1}/MPa^3 suggested by Barnes et al. (1971) is adopted. For simulations of indentation tests and ice-plate collision, n=4 is proper as the hydrostatic pressure is over 30MPa as calculated.

2.1.3 Delayed elastic stain

The delayed elastic deformation in axial direction can be represented in the time power law form. This can be described by part of Andarade's law in which the strain is the third power of time, $\varepsilon_t = \beta t^{1/3}$ (Glen, 1955; Schulson and Duval, 2009), where β is a parameter. In this model, Ashby and Duval's law (1985) is adopted,

$$\varepsilon_d = \frac{B\sigma}{E}\left[1-\exp\left(-\left(\frac{C\dot{\varepsilon}_v t}{\sigma/E}\right)^{1/m}\right)\right] \tag{11}$$

where σ is the axial stress, E is the elastic modulus, C=0.016 and m=3. In this model, the index of time is also 1/3. The delayed elastic strain is related with the viscous strain rate, thus is also dependent on temperature and confining pressure. As time goes on, the delayed elastic strain gradually approaches the maximum value $B\sigma/E$, and B is a parameter which can determine the maximum delayed strain. The maximum delayed elastic strain could be ten times higher than the instantaneous elastic strain (Cole, 1995; Duval, 1978), so the value of B should be around 10 or even greater.

Equation (11) is extended to three-dimensional form and the viscous strain rate is substituted by equation (9), then the deviatoric viscous strain can be expressed as,

$$e_{ij}^d = \frac{Bs_{ij}}{2G}\left[1-\exp\left(-\left(\frac{Cs^{n-1}t}{\eta^M/G}\right)^{1/3}\right)\right] \tag{12}$$

where $G = G^M$ is the shear modulus, s_{ij} and s are deviatoric stress component and effective stress as defined in viscous strain part.

Kelvin unit can represent the above equation. The total deviatoric stress is equal to the sum of the stresses produced by the spring and the dashpot in Kelvin unit as shown in Fig. 3,

$$2G^K e_{ij}^d + 6\eta^K t^{2/3}\dot{e}_{ij}^d = s_{ij} \tag{13}$$

$$G^K = G^M/B \tag{14}$$

$$2\eta^K = \left(\frac{(G^K)^2\eta^M}{CBs^{n-1}}\right)^{1/3} = \left(\frac{(G^K)^2\exp((Q+PV)/RT)}{2ABCs^{n-1}}\right)^{1/3} \tag{15}$$

where G^K, η^K and $\dot{e}_{ij}^d$ are the shear modulus, viscous coefficient and deviatoric strain rate component of the Kelvin body, respectively. Formula (12) and (13) are equivalent because the former is the analytical solution of the latter. The model shows that the delayed elastic constitutive relation is also nonlinear.

2.1.4 Plastic strain

The law of plastic deformation is described by the plastic potential theory, which is also one of the incremental plastic theories. In addition, the associated flow rule is adopted to specify that the direction of the plastic strain increment vector is normal to the yield surface. The plastic strain rates of the deviatoric and volumetric parts are respectively expressed as follows,

$$\dot{e}_{ij}^p = \dot{\lambda}\frac{\partial f}{\partial \sigma_{ij}} - \dot{\varepsilon}_{vol}^p \delta_{ij} \tag{16}$$

$$\dot{\varepsilon}_{vol}^p = \frac{\dot{\lambda}}{3}\left(\frac{\partial f}{\partial \sigma_{11}} + \frac{\partial f}{\partial \sigma_{22}} + \frac{\partial f}{\partial \sigma_{33}}\right) \tag{17}$$

where $\dot{\lambda}$ is the plastic consistency parameter and f is the yield function.

Formulas above in combination with the yield and failure criteria described in Section 2.2 below compose the viscoelastic-plastic constitutive model of ice. The viscoelastic and plastic strain rate parts are assumed to act in series. In the condition of the offshore structure subjected from creep load produced by floating ice cover moving slowly or by level ice under rising temperature against it, the strain rate is usually lower than 10^{-5} and time-dependent deformation can be fully developed. For the high-rate deformation with strain rate higher than 10^{-3}, the viscous part usually does not have enough time to develop, and the model will degenerate automatically to be nearly elastic-plastic.

2.2 Yield and failure criteria

For the plastic theory, establishing broadly effective yield and failure criteria is an essential task. Ice will undergo plastic volumetric deformation, and its yield stress is dependent on hydrostatic pressure, which is quite different from most metal materials and more like concrete and rock (Schulson, 2001). Studies

292 regarding the yield criterion of ice are insufficient as of yet, e.g., (Varsta, 1983, Und Polach et al., 2013, Kim
293 et al. 2011). Some studies have simulated the yield or failure phenomenon by using damage theory
294 considering that the damage begins to accumulate when stress begins to decline and that ice will fail at a
295 critical damage value. However, there remains a lack of unified and widely accepted damage criteria and
296 accumulation laws. Another approach is to use the yield surface method, which can reflect the stress or strain
297 state when ice material yields. Varsta (1983) summarised different criteria and suggested Tsai-Wu criterion is
298 suitable for ice problems. Derradji-Aouat et al. (2000, 2003, 2005, 2010) summarized the experimental
299 results of different kinds of ice and proposed a 3-D yield criterion based on Mroz's multi-surface concept,
300 which is relatively systematic and has a theoretical foundation. Timco and Frederking (1984) proposed an
301 n-type yield function to describe the behaviour of ice. Liu et al. (2011) and Shi et al. (2016) have prone
302 separately that the last two criteria are both Tsai-Wu type yield criterion and are hydrostatic pressure
303 dependent, because the equations can be deduced to the same form with Tsai-Wu equation. This yield
304 criterion can cover the test data within a certain range, which makes it a reasonable way to describe the yield
305 law of ice, although more data are needed to improve it. The Tsai-Wu yield surface is adopted here and can
306 be expressed as follows (Derradji-Aouat, 2003),

307 $$f(p,q)=\frac{3}{2}q^2-(a_0+a_1p+a_2p^2) \tag{18}$$

308 where a_0, a_1 and a_2 are constants; p is the hydrostatic pressure; and q is the octahedral shear
309 stress. The yield condition $f=0$ is represented by an ellipse on the $q-p$ plane. Equation (18) can be
310 written as follows,

311 $$\left(\frac{q}{q_{\max}}\right)^2+\left(\frac{p-\alpha}{p_{\max}}\right)^2=1 \tag{19}$$

312 where $p_{\max}$, $q_{\max}$ and α are important parameters affecting the shape of the elliptical line (see Fig. 4).
313 Note that the ellipse contains the origin; hence, the material in this model is able to support the tensile stress.

In the principle stress space, the failure criterion is represented by an ellipsoid of rotation about the hydrostatic pressure axis. Since the associated flow rule is adopted here, the plastic potential function is the same as the yield function, which determines the flow direction of plastic strain increments.

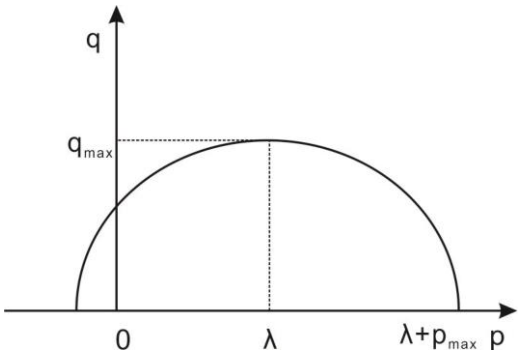

Fig. 4. Elliptical line of the Tsai-Wu yield criterion on the octahedral shear stress - hydrostatic pressure plane. Stresses out of the yield line evoke the plastic state, and stress will be mapped back to the yield surface through return mapping algorithm.

In the ice-structure interaction, ice will fail due to crushing or fracturing. Erosion technique is used to simulate the failure of ice in Finite Element Method. Once the element violates the failure criterion, it will be deleted. This technique is easy to implement and efficient. According to the classical theory of plasticity, no appreciable plastic deformation occurs in brittle failure. Nonetheless, plasticity theory has been used in descriptions of the brittleness of ice (Liu et al., 2011; Kolari, 2007; Shi et al. 2016). On the one hand, from the phenomenological point of view, the sudden drop of post-peak stress can be simulated with the use of the strain-softening concept in plastic theory (Kolari, 2007; Wang et al. 1997; Needleman, 1988). It is even feasible to extend the model to the ductile range by controlling the magnitude of strain softening, which is also a reason for using the viscoelastic plasticity to establish the model. On the other hand, since the erosion technique is used, the stress wave problem will lead to an inappropriate effect on the remaining elements in the simulation of elastic brittle failure of ice, in which case the plasticity concept can be adopted as a solution (Liu et al., 2011). Therefore, a proper failure criterion is important in the simulation of ice, as it determines

how much plastic strain is produced or how long the stress travels on the yield surface. In addition, the capacity of ice to resist compression is much stronger than to resist tension and thus should also be taken into account in the failure criterion. The empirical failure criterion established by Liu et al. (2011) and modified by Gao et al. (2015) was adopted. This failure criterion is based on equivalent plastic strain ε_{eq} and hydrostatic pressure σ_{vol} ,

if $\varepsilon_{eq}^{p} > \varepsilon_{f}$ or $\sigma_{vol} < p_{cut}$, the element fails,

$$\varepsilon_{eq}^{p} = \sqrt{\frac{2}{3}\varepsilon_{ij}^{p}\varepsilon_{ij}^{p}} \tag{20}$$

$$\varepsilon_{f} = \varepsilon_{0} + (\frac{\sigma_{vol}}{10^{8}} - 0.5)^{2} \tag{21}$$

where ε_{f} and p_{cut} are the thresholds of equivalent plastic strain and hydrostatic pressure, respectively. ε_{ij}^{p} is the component of the plastic strain tensor, and ε_{0} is the initial failure strain.

3. Numerical implementation and calibration of the program

3.1 Numerical implementation

The model is incorporated in LS-DYNA (Halquist, 2007) as a user-defined material subroutine, and the programme flow is shown in Fig. 5. At the beginning of each time step, the strain increment is imported from the software. It is assumed that only viscoelastic deformation has occurred at first and trial stresses were calculated. Then the yield function (18) is calculated. If $f \le 0$, the stress state is within the yield stress space and yield criterion is not met; then the trial results are real stresses in this time step and will be returned to the software. Otherwise ($f > 0$), the yield criterion is met and plastic deformation occurs. The trial stresses will be corrected through the return mapping algorithm. After several iterations, the stresses are mapped back to the yield surface and the results are returned at the current time step. The stresses travel on the yield surface over time until the failure criterion is satisfied. To calibrate the program and display the calculation process, single element simulations of constant

355 force loading and constant displacement loading will be conducted.

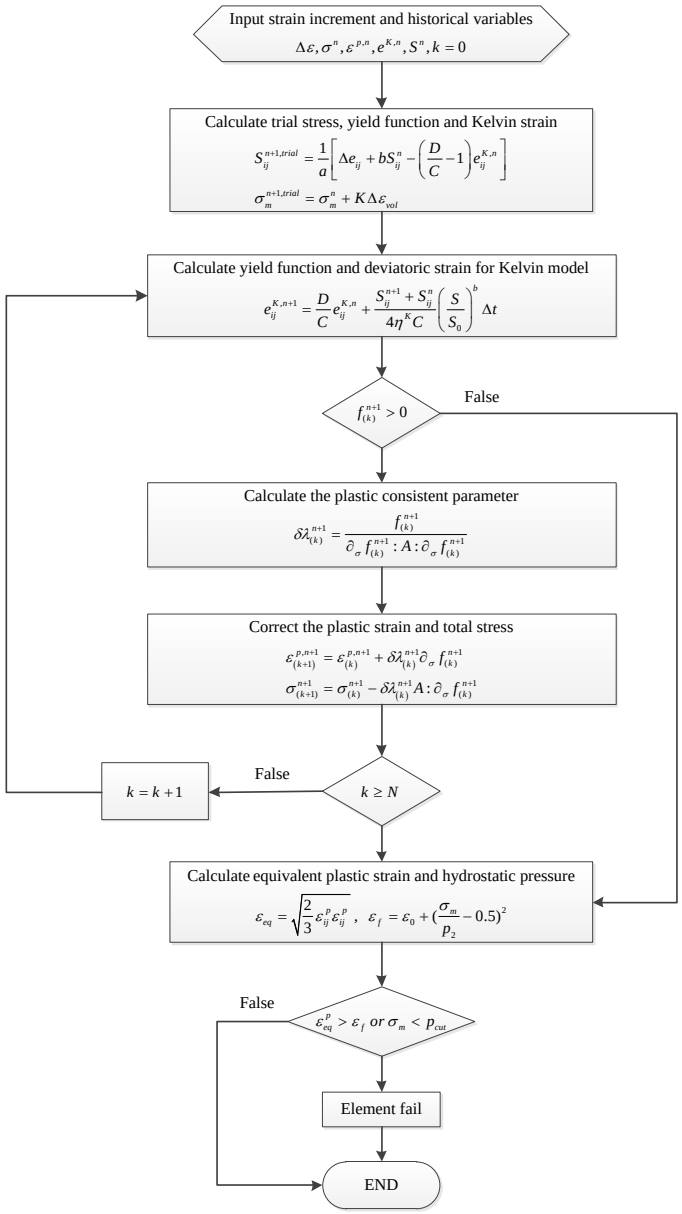

356

357 Fig. 5. Framework of the viscoelastic-plastic model. Viscoelastic deformation is assumed to occur and trial

358 stresses are calculated first. If $f \leq 0$, trial stresses are real stresses. Otherwise, trial stresses will be corrected

359 and iterated through the return mapping algorithm. The ice element will be deleted if the failure criterion is

360 satisfied.

361 **3.2 Constant force loading**

362 To calibrate the numerical program of the model and display the simulation capacity of

viscoelastic behaviour, a single-element test is conducted under constant force, including the loading and unloading processes. It is assumed that the model does not yield, and the results of the finite element analysis will be compared with the numerical results from Mathematica. A cubic solid unit is used, and constant loads of 2MN and 1MN are applied separately on the pairs of surfaces in the x direction and the other two directions as shown in Fig. 6 (left). The external loads are removed at 50 seconds to verify the simulating ability of the unloading scenario. A comparison of the numerical simulation results from LS-DYNA and Mathematica is illustrated in Fig. 6. The force on the right side refers to the difference value between the x direction and the other two directions. The finite element result agrees well with the Mathematica result, indicating that the numerical implementation process is correct.

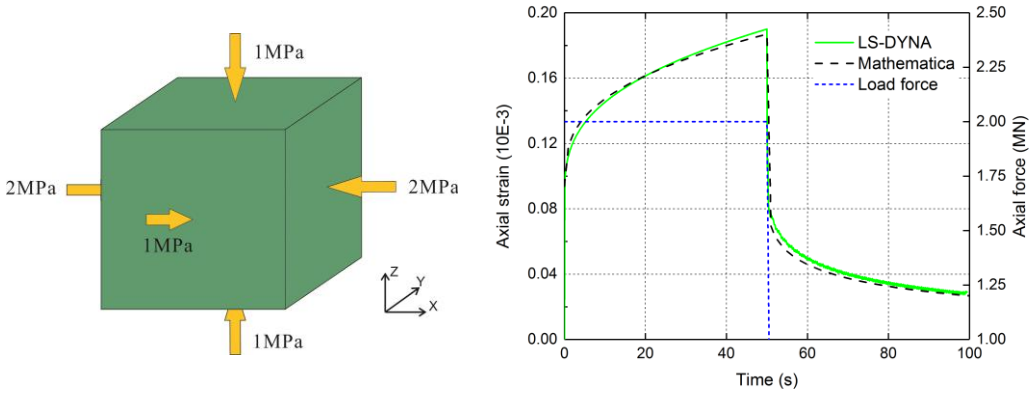

Fig. 6. Schematic diagram of single-element test with constant forces applied on the element surfaces, and the forces are withdrawn after t=50s (left). Comparison of the simulated creep curves in x direction from LS-DYNA and Mathematica, creep deformation is recovered after t=50s (right).

3.3 Constant displacement rate loading

This simulation displays the yield and failure process of the ice element. Four points on one surface of the ice element in x direction are fixed and the other four points are applied with a compressive displacement at the speed of 0.02m/s. Fig. 7 illustrates the stress development and failure

of the element (red line). At first, only viscoelastic deformation occurs. After the yield criterion is met, the stresses begin to flow on the yield surface, and the strain is developing at the same time, until the equivalent plastic strain meets the threshold value at the end of the red line. The dashed line indicates the stress flow on yield surface if the ice failure does not occur. The yield curve is elliptical and consistent with the description in Section 2.2.

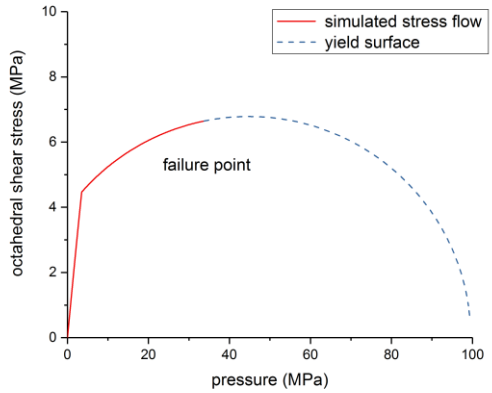

Fig. 7. Stress development and flow (red) on the yield surface under constant deformation rate loading. Intact yield surface (dashed) which stresses will flow on if ice does not fail.

4. Numerical examples and discussion

Numerical examples are described in this section to demonstrate the performance of the present model. First, a creep experiment is simulated to test the performance of the model to describe this rheological phenomenon. Second, the Pond Inlet medium-scale indentation test is simulated and the pressure-area curves are verified to demonstrate the model's ability to assess ice loads. Third, to verify the simulation ability of the model in brittle regions of high strain rates ($>10^{-3}$ / s), a collision scenario between ice and a rigid plate is simulated.

4.1 Creep experiments under tri-axial compressive conditions

4.1.1 Description of the creep experiments

Ice creep is a time-dependent behaviour related to the motion of crystal defects and is thermally

399 activated (Barratte and Jordaan, 2001). Since higher temperatures can accelerate the creep process, the creep
400 deformation of ice can be obvious at temperatures close to its melting point. A creep experiment is a
401 commonly used method to study this mechanical behaviour of ice. Xiao (1997) conducted a series of tri-axial
402 creep experiments using laboratory-prepared granular ice, and the test temperature was kept at $-10^{\circ}C$. The
403 seeds used to make ice samples were 2.00mm to 3.36mm. The ice samples were shaped into cylinders of
404 70mm in diameter and 175mm in length with minimal bubble content. During the tests, the ice samples were
405 subjected to confining pressure from all directions and an additional constant load in the axial direction.
406 Three typical test scenarios with different axial loads are simulated using the proposed model in this section.
407 To better illustrate the effectiveness and accuracy of the model proposed here, the simulation results of Shi et
408 al. (2017), who also simulated this creep test using a damage theory-based viscoelastic model, were adopted
409 for comparison.

410 4.1.2 Numerical model and material parameters

411 The finite element (FE) model is established using solid elements with one integration point as shown in
412 Fig. 8. The ice cylinder is fixed in the bottom, and constant pressures are applied on the side and top surfaces.
413 The confining pressure in the lateral direction is 10MPa, and the total axial pressures tested are 15MPa,
414 17MPa and 20MPa. The element size is 5mm×9mm×9mm . Other element sizes such as
415 3mm×6mm×6mm and 6mm×12mm×12mm are also tested and yield similar deformation as the
416 previous size. Hence, this simulation is not sensitive to element size due to the regular shape and small
417 deformation. The loading period is 20s, after which the external pressures are removed to investigate the
418 recovery of ice deformation, and the unloading phase is also set as 20s. As discussed in Section 2.1.2 and
419 Section 2.1.3, the main parameters of ice have been determined and are listed in Table 2. It should be noted
420 that n equals 3 in this part. Poisson's ratio is recommended by Timco and Weeks (2010). Parameters of the

421 yield function $a_0 / a_1 / a_2$ are 22.93, 2.06, -0.023 respectively according to Gao et al. (2015).

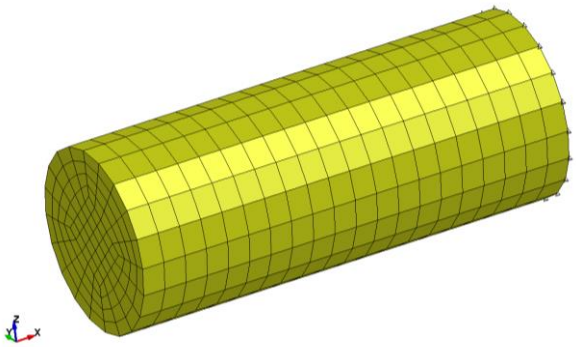

422

423 Fig. 8. Numerical model of a cylindrical ice sample with 70mm in diameter and 175mm in length. Confining

424 pressure of 10MPa is applied in lateral direction and axial pressures are 15MPa, 17MPa and 20MPa for

425 different cases.

426 Table. 2. Material parameters of the viscoelastic-plastic ice model used in simulation of creep experiments.

Parameter	**value**	**parameter**	**value**
Density	900 kg/m^3	Parameter C	0.016
Shear modulus of Maxwell unit (G^M)	5212MPa	Activation energy (Q)	78.6 kJ/m^2
Bulk modulus (K)	14862MPa	Activation volume (V)	32 cm^3 /mol
Poisson's ratio	0.343	Molar gas constant (R)	8.314
Exponential parameters (n)	3	Temperature (T)	263.15K
Parameter A	6.5E+8 MPa^{-3} gs^{-1}	Initial failure strain (ε_f)	0.01
Parameter B	15	Cut-off pressure (p_{cut})	-2.0MPa
Parameters in failure criterion ($a_0 / a_1 / a_2$)	22.93/2.06/-0.023		

427 4.1.3 Results and comparison to experiments

428 Fig. 9 illustrates the simulated curves of strain versus time at different axial stresses using the

429 viscoelastic-plastic model proposed here. The experimental results in the laboratory and simulation results of

Shi's (2017) viscoelastic model are also shown for comparison. The legend lists the effective stress. At the beginning, the instantaneous increase of strain represents the elastic deformation generated by the ice sample upon being subjected to external pressure. Then, the strain rises gradually over time, attributing mainly to the delayed elastic strain and viscous strain. In the loading phase, the curves calculated from this model agree well with those of the experimental results under the three stress levels. At the moment of 20s, the creep strain drops rapidly with the removal of the external force, then decreases slowly with time. The simulated recovering strains in unloading phase is in good agreement with the experimental results. Although the strain curve under effective stresses of 5MPa and 7MPa are slightly lower than the experimental value, the 10MPa curves correspond well. Compared to the viscoelastic model of Shi et al. (2017), the new proposed model yields results that are more consistent with experiments especially for 10MPa, and the distribution in relation times is well simulated. Shi's model and the viscoelastic part of the material model proposed in this paper are both established on Burgers model, but the construction ways are different, thus the descripted nonlinear strain-stress relations are different. The viscoelastic part of our model is based on Glen's law (1955) and Ashby and Duval's law (1985) and this method is prone to be effective, simulating the experimental phenomenon very well. The recovery curves of unloading phase correspond well to the experimental results, showing that the deformation components (elastic, delayed elastic and viscous deformation) are well described.

The nonlinearity of creep is illustrated by the nonlinear behaviour of the strains in response to different stress levels at the same time. According to the experimental results, no obvious plastic deformation occurred in the ice samples; otherwise, the strain would increase rapidly in a short period of time. In the numerical simulation of loading phase, the plastic strain is not triggered, which is in agreement with the experimental results. Thus, the simulation of this scenario using this model is realistic, and the unrecoverable strain

represents viscous deformation rather than plastic deformation. Corresponding to Section 2.1, the instantaneous drop at the moment of 20s represents the recovery of elastic strain, and the gradual decline in unloading phase represents the recovery of delayed elastic strain.

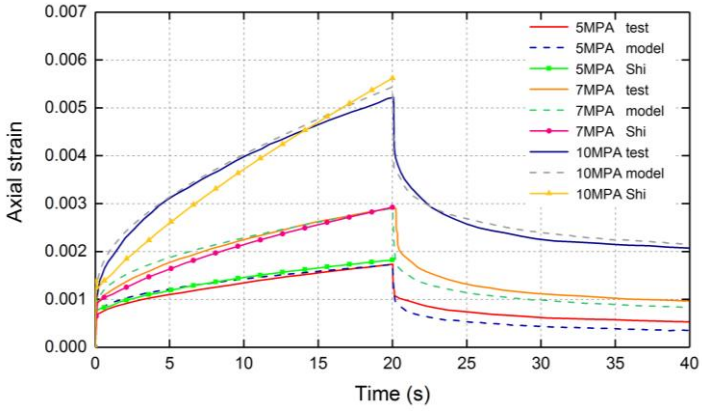

Fig. 9. Simulated strain-time curves using the viscoelastic-plastic material model (dashed) proposed here and viscoelastic model of Shi et al. (2017) (solid with dots), and experimental curves (solid, smooth) under different differential stresses (5MPa, 7MPa, 10MPa). External forces are removed at t=20s.

4.2 Pond Inlet indentation tests

4.2.1 Description of the indentation tests

Indentation tests can be used to investigate the failure mechanism of ice and obtain the contact force or pressure. Simulating indentation tests and comparing the contact force and pressure-area curves is a direct way to verify the accuracy of the proposed material model. For the indentation tests at laboratory scale, the contact areas are generally several square centimetres. It is challenging to extend the results to the ice-ship interaction analysis because of the size effect. Mobil Oil Canada (Kennedy, 1990; Johnson and Benoit, 1987) conducted a series of medium-scale indentation experiments on a grounded iceberg near Pond Inlet in 1984, and the maximum contact area reached 3m^2, which approached the size in full-scale ice-ship interactions. The Pond Inlet indention test with the maximum indenter is simulated in this section, and the simulation result of Liu et al. (2011) for the same test using an elastic-plastic model is also presented for comparison.

In Pond Inlet tests, a series of tunnels were excavated into the iceberg and the indenter system was positioned in the tunnel, and different sizes of spherical indenters were controlled to press into the vertical wall driven by the hydraulic system. Pressure cells were arranged on the face of the indenters to measure the local pressure of the indenting process, enabling the contact force to be obtained. A schematic of the experimental scenario and the corresponding numerical model is shown in Fig. 10. At beginning of the Pond Inlet test, the indenter was pressed towards the ice surface at constant velocity of 0.1m/s, and upon reaching the surface, the penetrating displacement $x(t)$ was imposed on the indenter as a quarter sine curve,

$$x(t) = x_0 \sin(\omega t) \tag{23}$$

where x_0 is the maximum penetration distance, ω is the frequency of motion, and t is time. The velocity of the indenter varies from initial maximum value to zero, which represents the slowing down of the ice or ship after impacting each other. The whole test lasted for 3.6s.

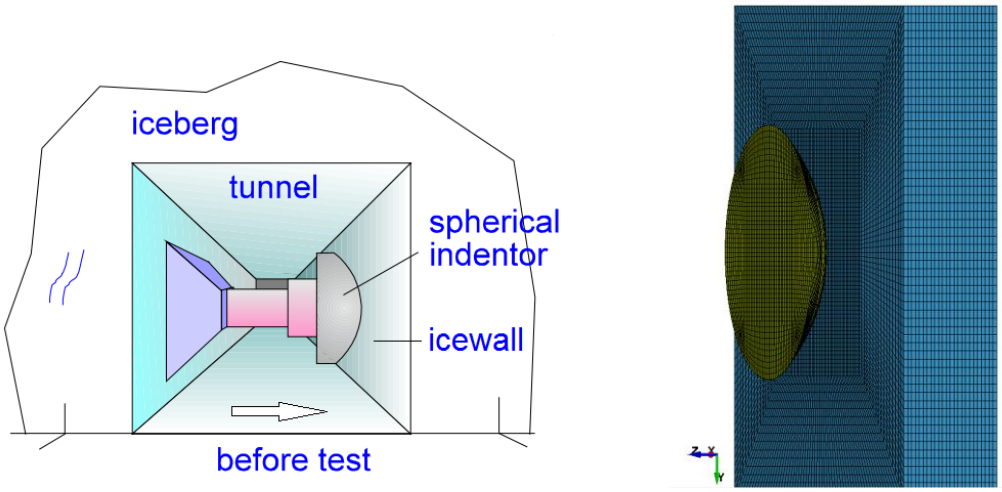

Fig. 10. Schematic diagram of the Pond Inlet experimental scenario (left) (Canada, 1994), the spherical indenter was placed inside the ice tunnel and pressed against the ice wall with the penetrating displacement as a quarter sine curve. Finite element models of the rigid indenter (yellow) and the ice wall (blue) with thickness of 1.2m and length and width of 6m (right).

4.2.2 Numerical model and material parameters

Compared to the iceberg, the stiffness of the indenter is much higher. In the FE model, the indenter is established as a section of rigid sphere with the radius of 2.3m, and the ice is modelled as a cuboid with height of 1.2m and length and width of 6m. The solid elements with one integration point are adopted. The nodes at the back of the ice wall are fixed, and the velocity is imposed on the indenter. An automatic contact algorithm is utilized between ice and indenter. An eroding contact algorithm is utilized for the iceberg; thus, the ice element will be deleted once it fails. The static and dynamic coefficients of friction are 0.15. Considering the relatively higher hydrostatic pressure (higher than 30MPa), n=4 is more proper. And the temperature T=253.15K. The other material parameters are the same as those in the simulation of creep experiments.

The hexahedral mesh grids are structured. The grids in the central part of ice are denser, and the surrounding grids are sparse to ensure the accuracy and efficiency of calculation. To select the appropriate element size, four mesh sizes (100mm×100mm×100mm, 75mm×75mm×75mm, 50mm×50mm×50mm, 30mm×30mm×30mm) in the middle part are tested.

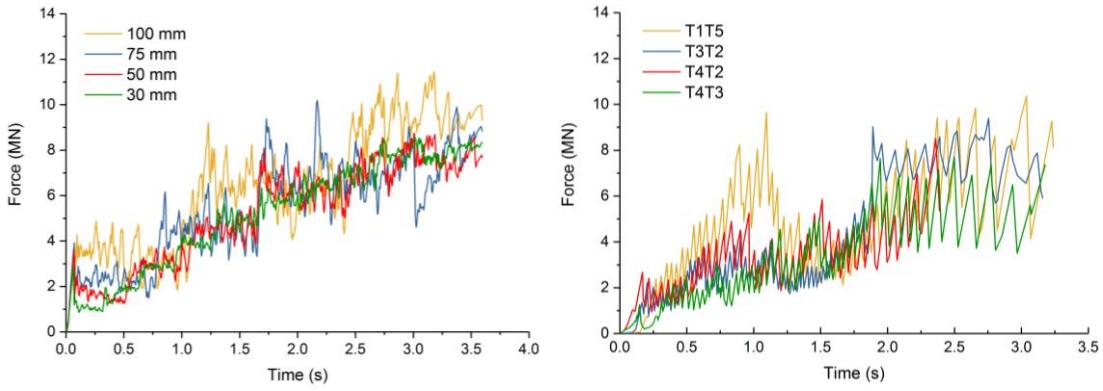

Fig. 11. Simulated contact force-time curves of Pond Inlet indentation tests using finite element model of ice wall with different element sizes (left). Experimental force-time curves of Pond Inlet indentation tests using the spherical indenter with the radius of 2.3m (right).

4.2.3 Results and comparison to experiments

505 The calculated curves of force versus time of different mesh sizes are illustrated in Fig. 11 (left). Smaller
506 elements lead to smaller fluctuations of the force curve and higher computational costs. The difference in
507 contact force of mesh size between 100mm and 75mm is larger, while the results of 50mm and 30mm are
508 similar. For a compromise between the effectiveness and efficiency of the calculation, 50mm is an ideal
509 choice. Fig. 11 (right) shows the in situ measurement results of a group of tests using the $3m^2$ indenter in
510 Pond Inlet test, and T1T5, T3T2, T4T2, and T4T3 are test numbers (Kennedy, 1990). The force of T1T5
511 before 1.5s is much higher than the others. Although the other curves have a similar trend, the obtained ice
512 loads are still different for different testing times. The saw-tooth response in the indention tests is thought to
513 be ice-induced oscillation as analysed by Browne et al. (2013) and O'Rourke et al. (2016), which is a
514 complex phenomenon. The numerical simulation with proper element size can capture the variation law of
515 the mean value of contact force over time.
516 Fig. 12 displays the distribution of hydrostatic pressure (left) and von Mises stress (right) as well as the
517 element erosion situation. As the indenter advances, the ice elements undergo the process from deformation
518 to failure. When meeting the failure criterion, the ice element will be deleted to simulate the process of ice
519 crushing. At 2.21s, a small pit forms as shown in Fig. 12. In the central position of the contact area of ice
520 (contacting with the top of the spherical indenter), the stress of ice is the highest. Moreover, the hydrostatic
521 stress reaches 35.52MPa, which is much higher than the maximum value of von Mises stress. In many
522 small-scale indentation tests (Brown et al. 2013, O'Rourke et al. 2016), it has been observed with the aid of
523 high-speed video that the damaged ice layer mainly exists in the contact area between ice and the indenter,
524 and the deformation of the ice is usually manifested as recrystallization and micro-fractures. Fig.11 shows
525 that only the stresses in the contact area are high, and the stresses in other areas are very low, especially for
526 the hydrostatic stress. This result is consistent with the observed experimental phenomenon.

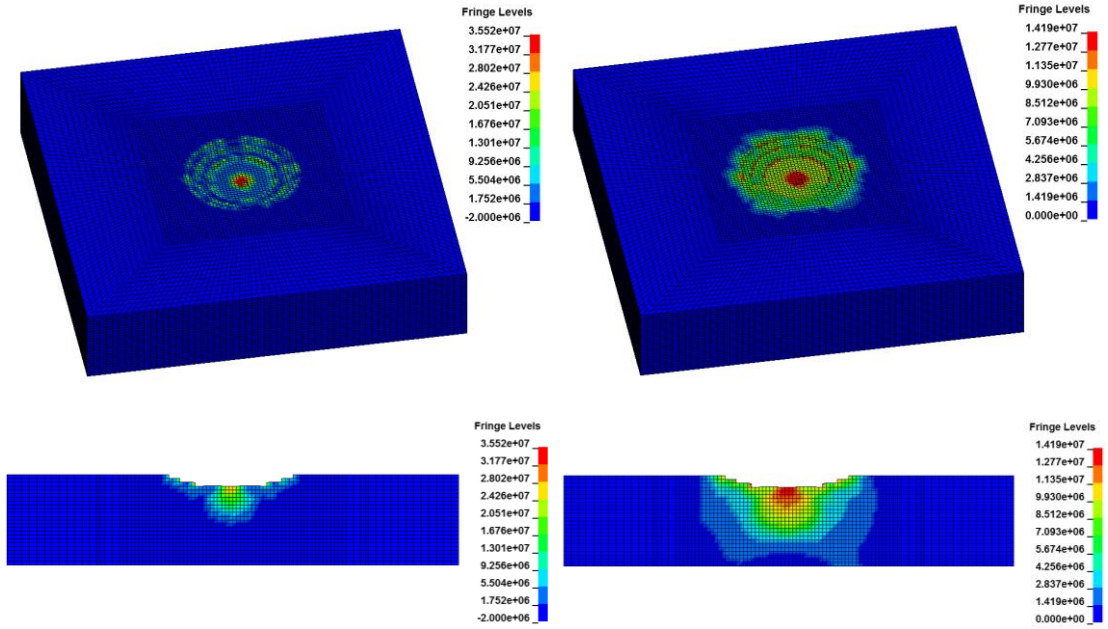

Fig. 12. Distribution of hydrostatic pressure [Pa] (left) and von Mises stress [Pa] (right) and element erosion of ice wall at t=2.21s. Contact surface between ice and indenter shown in first row, and middle vertical section of ice wall shown in second row. Red area represents high stress level and blue area represents low stress level.

The pressure-area relation is often used to evaluate the ice load on structures. The pressure-area curves of the numerical simulations and test data are compared and illustrated in Fig. 13. The pressure from numerical simulation is obtained by dividing the resultant force by the nominal contact area. When the contact area is less than $0.2m^2$, the simulation result of the viscoelastic-plastic model is higher than the test data. This is because the pressures from the tests are conservative, resulting from inaccurate control of the test start time according to Johnson and Benoit (1987). Pond Inlet's apparatuses were also used in Hobson's Choice indentation tests (Frederking et al., 1990) which obtained higher pressure in the small contact area using the same apparatus as the Pond Inlet, further illustrating the rationality of the simulation results. Over $0.2m^2$, the simulation result matches well with test results. Furthermore, the trend of simulation results is in accordance with the curve in the ISO/CD 19906 standard (2010), which is obtained from the pressure data of

543 the Molikpad structure (Masterson, et al. 2007), Gulf flat jack (Iyer and Masterson, 1987), Hobson's Choice
544 tests (Frederking et al., 1990; Gagnon, 1998) and Pond Inlet tests (Masterson et al. 1992).

545 Removing the Kelvin unit and the dashpot in the Maxwell unit, the viscoelastic-plastic (EVP) model
546 will degenerate to an elastic-plastic (EP) model, which is similar with the models of Gao et al. (2015) and Liu
547 et al. (2011). The values of the EP curve and EVP curve are very similar. This is because under high-speed
548 interactions of the ice and the indenter, the viscous and delayed elastic deformations of ice have not fully
549 developed in a short time before the failure of ice. In this condition, the performance of the
550 viscoelastic-plastic model is close to that of an elastic-plastic model. The pressure-area curves are also similar
551 to that of Liu's EP model as shown in Fig. 13, although the values are slightly different, probably due to
552 different parameters and meshing.

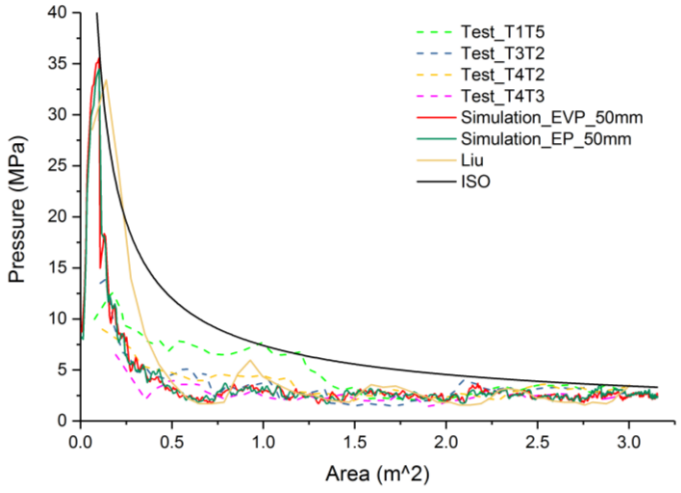

553

554 Fig. 13. Simulated pressure-area curves using viscoelastic-plastic model (solid, red) and elastic-plastic model
555 (solid, green), and experimental pressure-area curves (dashed) of Pond Inlet indentation tests. ISO standard
556 curve (solid, black) and simulated curve of Liu et al. (2011) (solid, yellow).

557 The calculation times of the models are also compared. The EP model takes 34 hours and 14 minutes to
558 finish the simulation, and the EVP model takes 42 hours and 53 minutes. The EVP model takes longer time
559 (8 hours and 39 minutes), but it is still in an acceptable range. For the actual interactions between ice and

structures, there are many conditions where the viscoelasticity of ice cannot be ignored, such as the piling up of ice around offshore platforms. The Kelvin unit and viscous element in the Maxwell unit of the EVP model representing the viscoelasticity will share the strain and produce lower stress than that of the EP model; therefore, this improvement gives the viscoelastic-plastic model the potential for better simulation of these conditions and a wider range of applicability.

4.3 Collision between spherical ice and a rigid plate

4.2.1 Description of the collision scenario and the numerical model

An ice-rigid plate collision scenario is simulated in this section to verify the material model's capacity to describe the brittleness of ice. The collision speed is 1m/s to ensure that the simulation is close to the situation of collision between ice and ship, and the deformation of ice is in the brittle region with high strain rates ($>10^{-3}/s$) (Schulson, 2001). The shape of the ice is a sphere, representing the mean model shape of the iceberg. A rigid plate is adopted to represent the Strength Design strategy (NORSOK Standard, 2004). If the calculated pressure does not exceed the rule requirements, then the actual pressure generated by the ice colliding with ships will also meet the requirements.

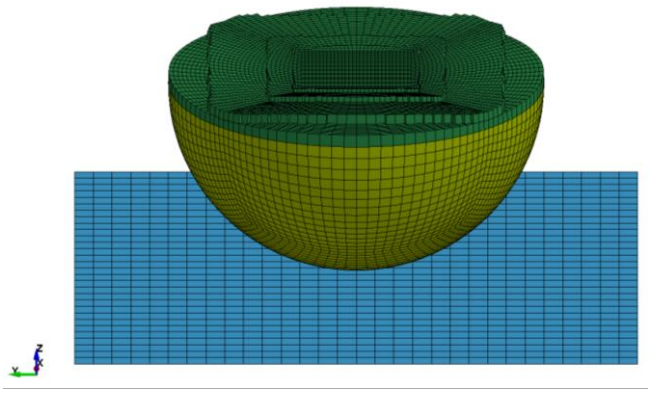

Fig. 14. Finite element model to simulate the collision between spherical ice (yellow) (radius of 1m) and a rigid plate (blue) (side length of 1.5m). Solid elements are used for ice and shell elements are used for the plate. The green part is fixed and the rigid plate moves towards ice at 1m/s.

The ice model is half a sphere with a radius of 1m, as shown in Fig. 14. The maximum penetration depth is 0.6m. Since the bottom of the sphere does not come into contact with the rigid plate, it is modelled as a rigid body and fixed. The rigid plate with the side length of 1.5m moves at a constant speed and collides with the spherical ice. An automatic contact algorithm is set, and the erosion technique is also adopted. The frictional coefficients are 0.15, and other ice material mechanical parameters, including the shear moduli and bulk modulus, are the same as those in Section 3.2. The temperature is assumed to be 253.15K. A parameter sensitivity analysis of mesh size (33mm×33mm×33mm , 22mm×22mm×22mm , 16.7mm×16.7mm×16.7mm) is performed. Fig. 15 illustrates the distribution of hydrostatic stress and von Mises stress, representing the volume stress and partial stress of ice, respectively, at the mesh size of 22mm×22mm×22mm .

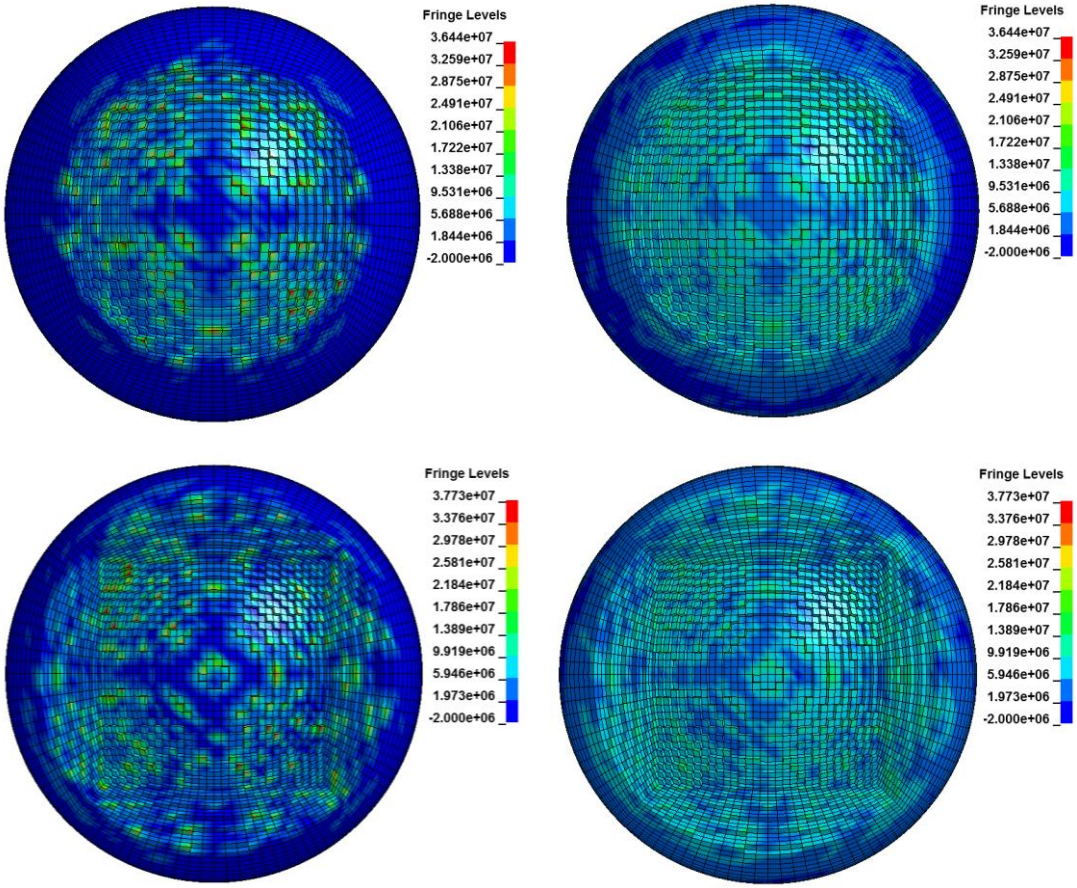

Fig. 15. Distribution of hydrostatic pressure [Pa] (left) and von Mises stress [Pa] (right) of the contact surface

591 of ice with steel plate. Penetration depths are 0.3m (first row) and 0.45m (second row). Red area represents

592 high stress level and blue area represents low stress level.

593 4.3.2 Results and discussion

594 Fig. 16 illustrates the pressure-area curve of the simulation, and different specifications and design

595 curves are also illustrated for comparison. According to the simulation results, once the spherical ice comes

596 into contact with the steel plate, the contact pressure is very large, then decreases rapidly with the penetration

597 distance and contact area increasing. When the contact area is larger than 0.5m^2, the pressure tends to reach a

598 stable value. This trend coincides well with the ISO standard (2010) and API (1995) curves, but the pressure

599 values are lower than those of the specifications. This finding is reasonable because the specification curves

600 take the upper limit of experiments and field test data (Masterson et al. 2007). Compared with the two

601 specification curves, the Molikpaq design curve (Masterson et al. 2007) is closer to the simulation results.

602 The simulated contact pressure fluctuates within a certain range along with the contact area, but the average

603 value agrees well with the pressure curve proposed by Timco and Sudom (2013). Timco's design curve is for

604 wide structures and takes the intermediate value of the test results of Molikpaq (east- and north-facing panels).

605 This finding further proves that the numerical simulation results are quite reasonable.

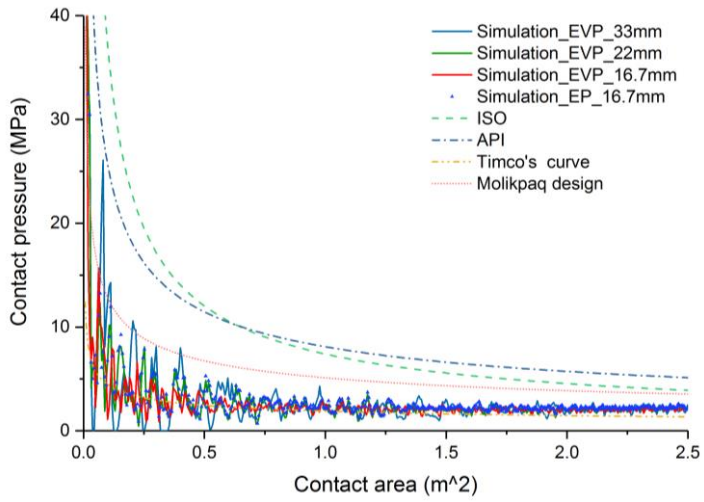

606

607 Fig. 16. Simulated contact pressure-area curves of ice-steel plate collision using viscoelastic-plastic model

608 (solid) with different mesh sizes and elastic-plastic model (dot), and different specifications and design curves
609 (dashed).

610 The fluctuation of the pressure curve derived from numerical simulation is due to the elements' erosion,
611 and it is more obvious when the contact area is smaller than $0.5m^2$ because the deletion of elements leads to
612 the change of contact force, and this change is amplified when the force is divided by a small contact area.
613 Unlike the massive ice in the simulation of indentation tests, the elements of the spherical ice are not well
614 confined. After contacting with the rigid plate, the ice elements at the top of the sphere fail rapidly under
615 pressure and are eroded; then, the contact force changes frequently in the small contact area. When the grid
616 density is larger, the pressure fluctuates more moderately, but the average pressure values of different grid
617 densities are similar, which indicates that the model has good robustness.

618 For the ice in the brittle region, the constitutive law is linear elastic before it fails, as shown in Fig. 1
619 (strain rate $= 0.2^{-1}/\mathrm{s}$). The numerical results of the elastic-plastic model, which are represented by
620 Simulation_EP_22mm in Fig. 16, are illustrated for comparison. The results show that most of the scattered
621 dots of Simulation_EP_22mm overlap with the Simulation_EVP_22mm curve. This finding proves that the
622 model has a good ability of simulating high-speed collision, the viscoelastic part will degenerate
623 automatically to become elastic. The proposed model retains a good capacity for describing the brittle
624 behaviour of ice.

625 **5. Conclusions**

626 A three-dimensional viscoelastic-plastic constitutive model is proposed in this paper to simulate the
627 behaviour of ice during the ice-structure interactions. The ice characteristics embodied in this model are more
628 comprehensive than the previous models, and verifications are made through three sets of comparisons
629 between numerical simulation results and those from tests. The main results are as follow:

630 The proposed model is composed of viscoelastic and plastic components acting in series. The
631 viscoelastic part is represented with a nonlinear Burgers model, in which the volumetric behaviour is
632 assumed to be elastic and the deviatoric behaviour is assumed to be viscoelastic and includes instantaneous
633 elastic, viscous and delayed elastic components. The viscous part is based on Glen's law (1955), and the
634 delayed elastic model is based on Ashby and Duval's equation (1985). Temperature and confining pressure
635 are included. The plastic part is evoked by a Tsai-Wu yield criterion that is hydrostatic pressure- and
636 octahedral shear stress- dependent. The incremental plastic theory and associated flow rule are adopted.

637 The numerical examples show that the present ice model yields well results and can reflect the
638 comprehensive characteristics of ice. Based on the laws summarised from experiments, the proposed model
639 can reflect the viscoelastic behaviour of ice well. In the simulation of creep experiments, the calculated
640 strain-time curves are consistent with the experimental results under different external loads and the strain
641 recovery in the unloading phase is simulated successfully. Combining with element erosion, the proposed
642 model also has a good capacity to simulate the ice-structure interaction in brittle region and predict the ice
643 load. In the simulation of Pond Inlet medium-scale indentation tests, the contact force and the average
644 pressure agree well with the experimental results. And the pressure-area curve of the ice-rigid plate collision
645 simulation is also in a reasonable range.

646 Compared to the elastic-plastic model, which is limited to high-speed interactions between ice and
647 structures, the proposed viscoelastic-plastic model includes viscoelasticity and thus has more potential
648 applications, e.g., the long-term piling up of ice around offshore platforms in Arctic regions, when the creep
649 deformation cannot be ignored. Moreover, this improvement makes the proposed model valuable for further
650 development to better simulate the post-peak softening behaviour and the ductile-brittle transition of ice.

651 **Acknowledgements**

This work is financially supported by the National Key Research and Development Program of China (Grant No.2016YFC0303405). The authors are sincerely grateful to this support.

Nomenclature

ε	total strain	K	bulk modulus
ε^e	instantaneous elastic strain	G^M	shear modulus of Maxwell unit
ε^d	delayed elastic strain	G^K	shear modulus of Kelvin unit
ε^v	viscous strain	η^M	viscous coefficient of Maxwell unit
ε^p	plastic strain	η^K	viscous coefficient of Kelvin unit
e_{ij}	deviatoric strain	a	exponent parameter of Maxwell unit
ε_{vol}	volumetric strain	Q	activation energy
σ	stress	υ	poisson's ratio
s_{ij}	deviatoric stress	δ_{ij}	delta function
p	volumetric stress	q	octahedral stress
$\dot{e}_{ij}$	total deviatoric elastic strain rate	R	molar gas constant
$\dot{e}_{ij}^e$	deviatoric elastic strain rate	$\dot{\lambda}$	plastic consistency parameter
$\dot{e}_{ij}^v$	deviatoric viscous strain rate	$f(p,q)$	yield function
$\dot{e}_{ij}^d$	deviatoric delayed elastic strain rate	$a_0/a_1/a_2$	constant parameters in yield function
$\dot{e}_{ij}^p$	deviatoric plastic strain rate	ε_{eq}	equivalent plastic strain
$\dot{\varepsilon}_{vol}$	volumetric elastic strain rate	ε_f	threshold of equivalent plastic strain
$\dot{\varepsilon}_{vol}^e$	volumetric elastic strain rate	ε_0	initial failure strain
$\dot{\varepsilon}_{vol}^p$	volumetric plastic strain rate	p_{cut}	threshold of hydrostatic pressure
V	activation volume	$A\,B\,C$	constant parameters

655 **References**

656 American Petroleum Institute. Exploration and Production Department. (1995). Recommended Practice for
657 Planning, Designing, and Constructing Structures and Pipelines for Arctic Conditions. American
658 Petroleum Institute.

659 Ashby, M. F., & Duval, P. (1985). The creep of polycrystalline ice. Cold Regions Science &
660 Technology, 11(3), 285-300.

661 Barnes, P., Tabor, D., & Walker, J. C. F. (1971). The friction and creep of polycrystalline ice. Proceedings of
662 the Royal Society A Mathematical Physical & Engineering Sciences, 324(1557), 127-155.

663 Barrette, P., & Jordaan, I. (2001). Compressive behavior of confined polycrystalline ice.

664 Browne, T., Taylor, R., Jordaan, I., & Gürtner, A. (2013). Small-scale ice indentation tests with variable
665 structural compliance. Cold Regions Science and Technology, 88, 2-9.

666 Budd, W. F., & Jacka, T. H. (1989). A review of ice rheology for ice sheet modelling. Cold Regions Science
667 & Technology, 16(2), 107-144.

668 Canada. Transport Canada. Canadian Coast Guard Northern, & Daley, C. (1994). Compilation of medium
669 scale ice indentation test results and comparison to ASPPR. National Research Council of Canada.

670 Cole, D. M. (1995). A model for the anelastic straining of saline ice subjected to cyclic loading. Philosophical
671 Magazine A, 72(1), 231-248.

672 Cole, D. M. (1998). Modeling the cyclic loading response of sea ice. International Journal of Solids and
673 Structures, 35(31-32), 4067-4075.

674 Derradji-Aouat, A. (2003). Multi-surface failure criterion for saline ice in the brittle regime. Cold Regions
675 Science & Technology, 36(1–3), 47-70.

676 Derradji-Aouat, A. (2005). Explicit FEA and constitutive modelling of damage and fracture in polycrystalline

677 ice-simulations of ice loads on offshore structures. In Proceedings of the International Conference on
678 Port and Ocean Engineering Under Arctic Conditions.
679 Derradji-Aouat, A. (2010). Critical roles of constitutive laws and numerical models in the design and
680 development of Arctic offshore installations. Publications.iot.nrc.ca.
681 Derradji-Aouat, A., Sinha, N. K., & Evgin, E. (2000). Mathematical modelling of monotonic and cyclic
682 behaviour of fresh water columnar grained s-2 ice. Cold Regions Science & Technology, 31(1), 59-81.
683 Durham, W. B., Heard, H. C., & Kirby, S. H. (1983). Experimental deformation of polycrystalline H2O ice at
684 high pressure and low temperature: Preliminary results. Journal of Geophysical Research: Solid Earth,
685 88(S01).
686 Duval, P. (1978). Anelastic behaviour of polycrystalline ice. Journal of Glaciology, 21(85), 621-628.
687 Frederking, R. M. W., Jordaan, I. J., & McCallum, J. S. (1990, August). Field tests of ice indentation at
688 medium scale: Hobson's Choice ice island 1989. In Proceedings of 10th International Symposium on
689 Ice, IAHR, Espoo, Finland (Vol. 2, pp. 931-944).
690 Gagnon, R. E. (1998). Analysis of visual data from medium scale indentation experiments at Hobson's
691 Choice ice island. Cold Regions Science & Technology, 28(1), 45-58.
692 Gagnon, R. E., & Gammon, P. H. (1995). Tri-axial experiments on iceberg and glacier ice. Journal of
693 Glaciology, 41(139), 528-540.
694 Gang, W., Ji, S. Y., Lv, H. X., & Yue, Q. J. (2006). Drucker-Prager yield criteria in viscoelastic-plastic
695 constitutive model for the study of sea ice dynamics1. Journal of Hydrodynamics, Ser. B, 18(6),
696 714-722.
697 Gao, Y., Hu, Z., Ringsberg, J. W., & Wang, J. (2015). An elastic–plastic ice material model for ship-iceberg
698 collision simulations. Ocean Engineering, 102, 27-39.

699 Glen, J. W. (1955). The creep of polycrystalline ice. Proceedings of the Royal Society of London, 228(1175),
700 519-538.
701 Halquist, J. (2007). LS-DYNA keyword user's manual version 971. Livermore Software Technology
702 Corporation, Livermore, CA.
703 Hill, B. T. (2006). Ship collision with iceberg database. In 7th International Conference and Exhibition on
704 Performance of Ships and Structures in Ice, 16-19.
705 ISO/CD 19906, 2010. Petroleum and Natural Gas Industries — Arctic Offshore Structures, ISO TC 67/SC
706 7/WG 8. Final Draft International Standard. International Standardisation Organization, Geneva,
707 Switzerland. 434 pp.
708 Iyer, S. H., & Masterson, D. M. (1987). Field strength of multi-year ice using thin-walled flat jacks. In Ninth
709 International Conference on Port and Ocean Engineering Under Arctic Conditions, University of Alaska,
710 Fairbanks, AK.
711 Jellinek, H. H. G., & Brill, R. (1956). Viscoelastic properties of ice. Journal of Applied Physics, 27(10),
712 1198-1209.
713 Ji, S. Y., Shen, H. T., Wang, Z. L., Shen, H. H., & Yue, Q. (2005). A viscoelastic-plastic constitutive model
714 with Mohr-Coulomb yielding criterion for sea ice dynamics. ACTA OCEANOLOGICA
715 SINICA-ENGLISH EDITION-, 24(4), 54.
716 Johnson, R. C., & Benoit, J. R. (1987). Iceberg impact strength. Proceedings of the 19th Annual Offshore
717 Technology Conference.
718 Johnston, M. E., Croasdale, K. R., & Jordaan, I. J. (1998). Localized pressures during ice–structure
719 interaction: relevance to design criteria. Cold regions science and technology, 27(2), 105-117.
720 Jones, S. J. (1982). The confined compressive strength of polycrystalline ice. Journal of Glaciology, 28(98),

171-178.

Jones, S. J., & Chew, H. A. (1983). Creep of ice as a function of hydrostatic pressure. The Journal of Physical Chemistry, 87(21), 4064-4066.

Jones, S. J., Gagnon, R. E., Derradji, A., & Bugden, A. (2003). Compressive strength of iceberg ice. Canadian journal of physics, 81(1-2), 191-200.

Jordaan, I. J. (2001). Mechanics of ice–structure interaction. Engineering Fracture Mechanics, 68(17-18), 1923-1960.

Jordaan, I., Li, C., Sudom, D., Stuckey, P., & Ralph, F. (2005). Principles for local and global ice design using pressure-area relationships. In Proceedings of the International Conference on Port and Ocean Engineering Under Arctic Conditions.

Kennedy, K. P. (1990). Dynamic activity and crushed ice behavior in medium-scale ice-structure interactions [microform]. Memorial University of Newfoundland.

Khon, V. C., Mokhov, I. I., Latif, M., Semenov, V. A., & Park, W. (2010). Perspectives of Northern Sea Route and Northwest Passage in the twenty-first century. Climatic Change, 100(3-4), 757-768.

Kim, E., Amdahl, J., & Løset, S. (2011). Development of ice failure and yield criteria for accidental limit state design. In Proceedings of the International Conference on Port and Ocean Engineering Under Arctic Conditions (No. POAC11-023).

Kolari, K. (2007). Damage mechanics model for brittle failure of transversely isotropic solids: Finite element implementation. VTT Technical Research Centre of Finland.

Kolari, K. (2013). Simulation of brittle failure of ice. In Proceedings of the 22th International Conference on Port and Ocean Engineering Under Arctic Conditions, POAC'13, Espoo, Finland, June 9–13, 2013, 1-12.

743 Kolari, K. (2017). A complete three-dimensional continuum model of wing-crack growth in granular brittle
744 solids. International Journal of Solids and Structures, 115, 27-42.
745 Lai, W. M., Rubin, D. H., Rubin, D., & Krempl, E. (2009). Introduction to continuum mechanics.
746 Butterworth-Heinemann.
747 Leclair, E. S., Schapery, R. A., & Dempsey, J. P. (1999). A broad-spectrum constitutive modeling technique
748 applied to saline ice. International Journal of Fracture, 97(1-4), 209-226.
749 Liu, Z., Amdahl, J., & Løset, S. (2011). Plasticity based material modelling of ice and its application to ship–
750 iceberg impacts. Cold Regions Science & Technology, 65(3), 326-334.
751 Masterson, D. M., D.E. Nevel, R.C. Johnson, J.J. Kenny , P.A. Spencer (1992). The medium scale iceberg
752 impact test program, Proceedings, IAHR Ice Symposium 1992, Banff, Alberta.
753 Masterson, D. M., Frederking, R. M. W., Wright, B., Karna, T., & Maddock, W. P. (2007). A revised ice
754 pressure-area curve. Recent Development of Offshore Engineering in Cold Regions----Proceedings of
755 the, International Conference on Port and Ocean Engineering under Arctic Conditions.
756 Mellor, M., & Cole, D. M. (1982). Deformation and failure of ice under constant stress or constant strain-rate.
757 Cold Regions Science and Technology, 5(3), 201-219.
758 Needleman, A. (1988). Material dependence and mesh sensitivity in localization problems. Computer
759 Methods in Applied Mechanics & Engineering, 67(1), 69-85.
760 NORSOK Standard N-004, 2004. Design of Steel Structures, Appendix A, Design Against Accidental
761 Actions.
762 O'Rourke, B. J., Jordaan, I. J., Taylor, R. S., & Gürtner, A. (2016). Experimental investigation of oscillation of
763 loads in ice high-pressure zones, part 1: Single indentor system. Cold Regions Science and
764 Technology, 124, 25-39.

765 Ortiz, R., Deletombe, E., & Chuzel-Marmot, Y. (2015). Assessment of damage model and strain rate effects
766 on the fragile stress/strain response of ice material. International Journal of Impact Engineering, 76,
767 126-138.
768 Ostreng, W., Eger, K. M., Fløistad, B., Jørgensen-Dahl, A., Lothe, L., Mejlænder-Larsen, M., & Wergeland, T.
769 (2013). Shipping in Arctic waters: a comparison of the Northeast, Northwest and trans polar passages.
770 Springer Science & Business Media.
771 und Polach, R. V. B., Ehlers, S., & Kujala, P. (2013). Model-scale ice—Part A: Experiments. Cold Regions
772 Science and Technology, 94, 74-81.
773 Rist, M. A., & Murrell, S. A. F. (1994). Ice triaxial deformation and fracture. Journal of Glaciology, 40(135),
774 305-318.
775 Saksala, T., Brancherie, D., Harari, I., & Ibrahimbegovic, A. (2015). Combined continuum damage-
776 embedded discontinuity model for explicit dynamic fracture analyses of quasi-brittle materials.
777 International Journal for Numerical Methods in Engineering, 101(3), 230-250.
778 Schulson, E. M., & Nickolayev, O. Y. (1995). Failure of columnar saline ice under biaxial compression:
779 Failure envelopes and the brittle-to-ductile transition. Journal of Geophysical Research: Solid Earth,
780 100(B11), 22383-22400.
781 Schulson, E. M. (2001). Brittle failure of ice. Engineering Fracture Mechanics, 68(17–18), 1839-1887.
782 Schulson, E., & Duval, P. (2009). Creep and fracture of ice. Cambridge University Press.
783 Shi, C., Hu, Z., Ringsberg, J., & Luo, Y. (2016). Validation of a temperature-gradient-dependent
784 elastic-plastic material model of ice with finite element simulations. Cold Regions Science &
785 Technology, 133(1), 15-25.
786 Shi, C., Hu, Z., Ringsberg, J., & Luo, Y. (2017). A nonlinear viscoelastic iceberg material model and its

787 numerical validation. Proceedings of the Institution of Mechanical Engineers, Part M: Journal of
788 Engineering for the Maritime Environment, 231(2), 675-689.
789 Sinha, N. K. (1978). Rheology of columnar-grained ice. Experimental Mechanics, 18(12), 464-470.
790 Sinha, N. K. (1982). Constant strain-and stress-rate compressive strength of columnar-grained ice. Journal of
791 Materials Science, 17(3), 785-802.
792 Snyder, S. A., Schulson, E. M., & Renshaw, C. E. (2016). Effects of prestrain on the ductile-to-brittle
793 transition of ice. Acta Materialia, 108, 110-127.
794 Taylor, R. S., & Jordaan, I. J. (2014). Damage and Fracture during Contact between a Spherical Indenter and
795 Ice: Experimental Results and Finite Element Simulations. In Key Engineering Materials (Vol. 577, pp.
796 609-612). Trans Tech Publications.
797 Timco, G. W., & Frederking, R. M. W. (1984). An investigation of the failure envelope of
798 granular/discontinuous-columnar sea ice. Cold Regions Science & Technology, 9(1), 17-27.
799 Timco, G. W., & Sudom, D. (2013). Revisiting the Sanderson pressure–area curve: defining parameters that
800 influence ice pressure. Cold Regions Science & Technology, 95(11), 53-66.
801 Timco, G. W., & Weeks, W. F. (2010). A review of the engineering properties of sea ice. Cold Regions
802 Science & Technology, 60(2), 107-129.
803 Varsta, P. (1983). On the mechanics of ice load on ships in level ice in the baltic sea.
804 Wang, W. M., Sluys, L. J., & De Borst, R. (1997). Viscoplasticity for instabilities due to strain softening and
805 strain-rate softening. International Journal for Numerical Methods in Engineering 40 (20), 3839-3864.
806 Xiao, J. (1997). Damage and fracture of brittle viscoelastic solids with application to ice load models.
807 Memorial University of Newfoundland.
808 Zhou, Z., Ma, W., Zhang, S., Mu, Y., Zhao, S., & Li, G. (2016). Yield surface evolution for columnar ice.

809 Results in Physics, 6, 851-859.